ASSESSING THE POTENTIAL OF CHEMILUMINESCENCE TO CHARACTERIZE NO FORMATION IN AMMONIA-METHANE PREMIXED FLAT FLAMES

***Shijia LIU, Zhicong LI**[*]*

School of Mechanical and Power Engineering, Zhengzhou University, Zhengzhou, Henan 450001, China

[*]Corresponding author; E-mail: zcli@zzu.edu.cn

The NO formation characteristics in laminar NH_3-CH_4 premixed flat flames and their relationship with chemiluminescence are numerically investigated across different ammonia blending ratios (X_{NH3}, 0-1.0) and equivalence ratios (φ, 0.7-1.3). The applicability of the reaction mechanism and flame model in predicting the formation of NO and $OH^*/NH^*/CH^*/CO_2^*/NH_2^*$ radicals is verified. The results show that the peak flame temperature gradually increases with increasing X_{NH3}, while it first increases and then decreases with increasing φ. For NO mole fraction, increasing X_{NH3} affects the competition among reactions R763 ($HNO + H = NO + H_2$), R765 ($HNO + OH = NO + H_2O$), and R842 ($NH + NO = N_2O + H$) by altering the HNO and NH mole fractions, causing NO to first increase and then decrease. Moreover, increasing φ continuously reduces the formation rate of NO via R765. For $OH^*/NH^*/CH^*/CO_2^*/NH_2^*$ mole fractions, as X_{NH3} increases, NH^* and CH^* peak at $X_{NH3} = 0.3$ and 0.6, respectively; OH^* and NH_2^* increase monotonically, while CO_2^* decreases. With increasing φ, the peaks of $OH^*/NH^*/CH^*/CO_2^*$ appear at $\varphi = 1.0/1.0/1.0/0.8$, while NH_2^* continues to rise. Regarding the relationship between NO and chemiluminescence, a nearly monotonic relationship is observed between the peak mole fraction of NO and CO_2^*. With varying X_{NH3}, similar relationships exist between NO and the ratios of CO_2^*/OH^*, CO_2^*/NH^*, and CO_2^*/CH^*, but these relationships break down at high X_{NH3}. Over a wide φ range, the NH_2^*/CO_2^* ratio shows good potential for predicting NO formation and emission. This study facilitates accurate monitoring and emission control of NO_x in NH_3-blended combustion systems.

Key words*: Ammonia, NO, chemiluminescence, premixed flat flame, kinetic analysis.*

1. Introduction

To reduce greenhouse gas emissions and mitigate global warming [1,2], ammonia (NH_3), a carbon-free fuel, has regained considerable attention from combustion researchers [3-5]. Compared to hydrogen (H_2), NH_3 offers advantages in production, storage, and transportation safety [6,7]. However, NH_3 combustion faces significant challenges [8], including a low flame speed, high ignition energy requirements, and elevated nitrogen oxide (NO_x) emissions. To address these limitations, NH_3 is often blended with hydrocarbon fuels, such as natural gas, to enhance flame stability and optimize emission characteristics [9-11].

The inherently high NO_x emissions remain a major obstacle to the practical application of NH_3 as a fuel. To address this issue, researchers have investigated the emission characteristics, formation pathways, and measurement techniques related to NO_x in NH_3 combustion. To clarify the combustion chemistry and NO_x formation mechanisms of NH_3, Li *et al.* [12] developed a detailed reaction mechanism applicable to $NH_3/H_2/CH_4$ flames. Their results demonstrated that the NO mole fraction is elevated in high-temperature regions near the stoichiometric zone, while NO_2 dominates in fuel-lean regions, highlighting the distinct patterns of NO_x in different combustion regions. Ahmed *et al.* [13] analyzed recent experimental and numerical advancements in turbulent NH_3 and NH_3-blended combustion technologies. They demonstrated that blending highly reactive fuels (H_2, CH_4, etc.) with NH_3 in premixed flame burners enhances flame stability, but also increases NO_x emissions due to elevated mole fractions of H and OH radicals.

Accurate measurement of NO_x emissions is essential in most studies on NH_3-blended flames. Planar Laser-Induced Fluorescence (PLIF), a powerful diagnostic tool for scalar measurements in combustion systems, has been successfully used to measure NO and OH intensities in NH_3-air flames [11,14]. Additionally, NO_x emissions can be measured using instruments such as Fourier Transform Infrared Spectroscopy (FT-IR) and flue gas analyzers [10,15]. However, both PLIF and FT-IR have limitations, including high cost, limited temporal resolution (for FT-IR), and poor adaptability to dusty or vibrating environments. Flue gas analyzers also face challenges such as cross-sensitivity to NH_3/H_2O interference, frequent calibration requirements, and reduced accuracy in H_2O-laden gases. In addition to experimental approaches, numerical modeling based on NH_3 combustion mechanisms can also be used to predict NO_x emissions [16-18]. However, issues such as high computational cost, limited prediction accuracy, and incomplete reaction mechanisms remain to be addressed.

To develop low-cost NO_x monitoring technologies, Zhu *et al.* [19] demonstrated a monotonic relationship between OH^* chemiluminescence intensity (measured in the reaction zone) and the overall NO mole fraction in NH_3-H_2-air swirl flames. Chemiluminescence is the spontaneous emission of radiation by excited radicals formed through chemical reactions [20-22]. Despite the harsh combustion environment, chemiluminescence-based NO_x monitoring technology maintains high accuracy and can be used in situations where traditional on-site monitoring is impractical [23]. As a result, optical diagnostics based on chemiluminescence are applied to analyze various combustion characteristics [24]. Most commonly, CH^* and OH^* chemiluminescence indicate the flame surface position and show a positive correlation with heat release rates [25,26].

Recent studies have investigated the chemiluminescence characteristics of NH_3-blended flames to facilitate the application of chemiluminescence-based diagnostics. The key excited radicals contributing to the chemiluminescence of NH_3-CH_4 flames across the ultraviolet (UV) and visible ranges include NO^*, OH^*, NH^*, CN^*, CO_2^*, CH^*, and NH_2^* [27]. Similar to the monotonic relationship between OH^* chemiluminescence intensity and NO mole fraction reported in Ref. [19], Pugh *et al.* [28] conducted time-resolved OH^*, NH_2^*, and NH^* chemiluminescence measurements on NH_3-blended flames in a fuel-flexible burner and emphasized the importance of the NH_2^* radical as a strong indicator of NO depletion in flames. Zhu *et al.* [29] investigated the chemiluminescence characteristics of NH_3-CH_4 premixed flames over a wide range of equivalence ratios and strain rates. They established a comprehensive database of chemiluminescence intensity and proposed that the ratios of CN^*/OH^* and CN^*/NO^* serve as potential indicators of the equivalence ratio in NH_3-blended flames. Additionally, Guiberti *et al.* [30] developed a Gaussian process regression (GPR) algorithm to predict the equivalence ratio and NH_3 mole fraction in NH_3-CH_4-air premixed flames based solely on OH^*, NH^*, CN^*, and CH^* chemiluminescence intensities. This work laid the foundation for developing non-invasive chemiluminescence-based sensors for real-time monitoring of NH_3-blended flames. In general, current chemiluminescence-based NO emission investigations have predominantly focused on simplified relationships between peak OH^* and NH_2^* radical concentrations with NO formation/depletion. However, the qualitative relationship between other excited radicals/chemiluminescence intensity ratios and NO formation/depletion characteristics in NH_3-blended flames remains underexplored. Because OH^* chemiluminescence is located in the UV band (310 nm), and the signal-to-noise ratio (SNR) and cost of UV sensors are usually higher than those of visible light sensors, it is not suitable for large-scale industrial diagnostic applications. As for NH_2^* chemiluminescence, although it appears within the visible range (630 nm), it overlaps with H_2O^* and NO_2^* chemiluminescence [22,27], complicating quantitative analysis. As a result, the relationship between the remaining chemiluminescence and NO still requires further investigation.

Given the above background, this numerical study focuses on NO formation characteristics and their relationship with chemiluminescence in laminar NH_3-CH_4 premixed flat flames, motivated by two considerations: (1) investigating the effects of the NH_3 blending ratio (X_{NH3}) and equivalence ratio (φ) on flame temperature and NO formation characteristics, and (2) assessing the potential of $OH^*/NH^*/CH^*/CO_2^*/NH_2^*$ chemiluminescence to characterize NO emission/mole fraction, as these species dominate in the target flames. Therefore, the reactions of the above-mentioned excited radicals are incorporated into an existing gas-phase NH_3-CH_4 mechanism. Laminar NH_3-CH_4 premixed flat flames with different NH_3 blending ratios (X_{NH3}, 0-1.0, interval 0.1) and equivalence ratios (φ, 0.7-1.3, interval 0.1) are studied. Some key conclusions are discussed to facilitate accurate monitoring and emission control of NO_x in NH_3-blended combustion systems.

2. Numerical model

2.1. Reaction mechanism

To simultaneously model the formation of NO and $OH^*/NH^*/CH^*/CO_2^*/NH_2^*$ radicals in NH_3-CH_4-air flat flames, the gas-phase mechanism developed by Liu *et al.* [31] , known as the HUST-NH_3 mechanism, is selected as the base mechanism. Additionally, reaction pathways, thermodynamic data, and transport properties for the above-mentioned excited radicals are incorporated from Ref. [32,33]. Modifications to the pre-exponential factors in OH^*- and NH^*-related reactions are implemented following the recommendations of Capriolo *et al.* [23] and Issayev *et al.* [34], to enhance the accuracy in predicting their mole fractions and spatial distributions. For clarity in subsequent discussions, the modified mechanism is referred to as the HUST-C mechanism.

2.2. Flame condition and modeling

The premixed flat flame burner model in ANSYS Chemkin 17.0 is used to numerically simulate NH_3-CH_4-air premixed flat flames. The model simultaneously solves the continuity, momentum, species, and energy conservation equations. The gas-phase reactions are embedded in the conservation equations in the form of rate terms rather than as independent solution objects. A schematic of the flame model is shown in Fig. 1, and the one-dimensional computational domain is indicated by the red dashed line. Specifically, the burner plug has a diameter of 60 mm, and the stagnation plane is positioned 20 mm above the burner surface to suppress flickering of the post-flame gases. An NH_3-CH_4-air mixture (21% O_2 + 79% N_2) is injected into the burner, with varying NH_3 blending ratios (X_{NH3} ranging from 0-1.0) and equivalence ratios (φ ranging from 0.7-1.3), as summarized in Tab. 1. In detail, the NH_3 blending ratio (X_{NH3}) is defined as:

$$X_{NH3} = \frac{\chi_{NH3}}{\chi_{NH3} + \chi_{CH4}} \times 100\% \tag{1}$$

where χ refers to the mole fraction of NH_3 and CH_4 in the fuel stream (excluding air). The initial gas temperature and pressure are set to ambient conditions (294 K and 1 atm). Detailed model parameters and configurations follow those in Ref. [35].

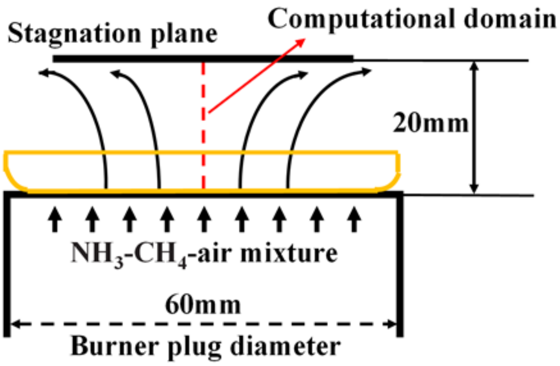

Figure 1. Schematic of the numerical NH_3-CH_4-air premixed flat flame model.

Table 1 Numerical conditions for NH_3-CH_4-air premixed flat flame

NH_3 blending ratio, X_{NH3}	Equivalence ratio, φ	Flow rate (cm/s)
0-1.0, $\Delta X_{NH3} = 0.1$	0.9	5
0.6	0.7-1.3, Δφ = 0.1	5

3. Results and discussion

3.1. Numerical benchmarking

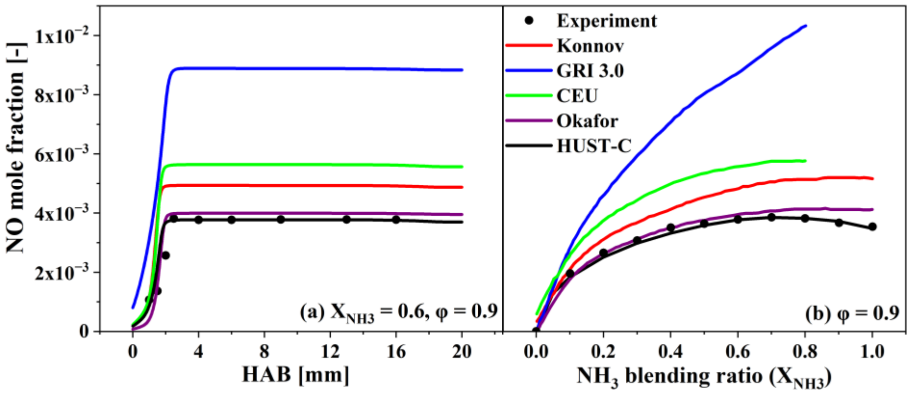

Figure 2. Comparison of numerical (peak) NO mole fraction modeled by different mechanisms with experimental results. (a: X_{NH3} = 0.6 and φ = 0.9, b: X_{NH3} ranges from 0 to 1.0)

To validate the accuracy of the gas-phase mechanism and flame model, numerical results from the HUST-C mechanism are compared with those from other mechanisms (GRI 3.0, Okafor [16], CEU [18], and Konnov [36]) as well as with experimental data [35]. Fig. 2(a) shows the NO mole fraction at different heights above the burner (HAB), modeled using various mechanisms at X_{NH3} = 0.6 and φ = 0.9. The numerical results from the HUST-C mechanism agree well with the experimental data, particularly in terms of peak values and the overall trend. Fig. 2(b) shows the peak NO mole fraction at φ = 0.9 with varying X_{NH3}. The peak NO mole fraction predicted by the HUST-C mechanism closely matches the experimental results, exhibiting a trend that increases and then decreases with rising X_{NH3}. In contrast, the other mechanisms fail to capture the decreasing trend in peak NO mole fraction at high X_{NH3} values (0.7-1.0). These results indicate that the HUST-C mechanism is applicable to NH_3-CH_4 premixed flat flames.

Furthermore, NH_3-CH_4-air counterflow premixed flames are numerically modeled using the HUST-C mechanism to verify its feasibility in predicting the formation of OH^*/NH^*/CH^*/CO_2^*/NH_2^* radicals. Specifically, the simulation results obtained using this mechanism are compared with experimental data from Zhu *et al*. [29] and numerical predictions from Konnov *et al*. [33], as shown in Fig. A.1 of Appendix A. The comparison results demonstrate that the numerical modeling using the HUST-C mechanism exhibits better agreement with the experimental data than the predictions by Konnov *et al*., as the original mechanism (HUST-NH_3 mechanism) has good predictive accuracy for NH_3-blended flames. Additionally, this study modifies the pre-exponential factor for OH^*- and NH^*-related reactions. In summary, the premixed flat flame model and the HUST-C mechanism are applicable to NH_3-CH_4 flames for capturing the formation characteristics of NO and excited radicals.

3.2. Temperature

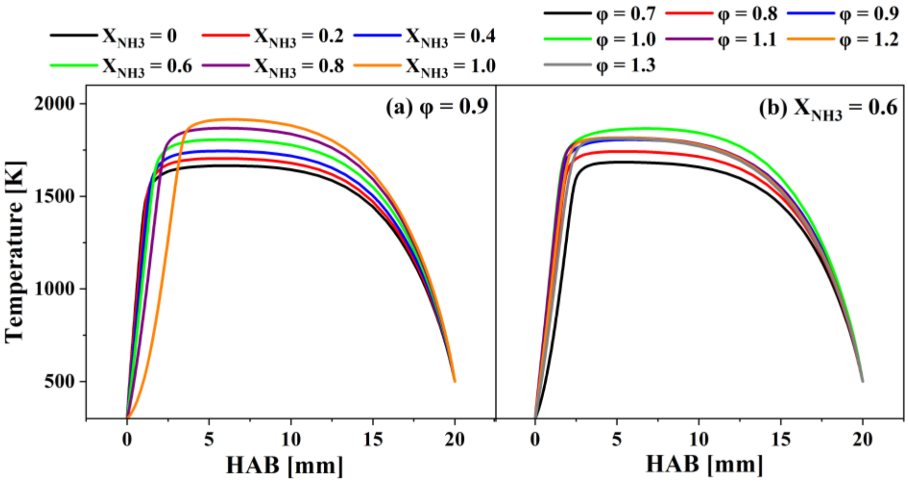

Figure 3. Temperature profiles. (a: φ = 0.9, X_{NH3} ranges from 0 to 1.0, b: X_{NH3} = 0.6, φ ranges from 0.7 to 1.3)

Fig. 3 presents the temperature distributions for all cases. The temperature profiles generally rise initially, then gradually decline, and finally drop sharply near HAB = 20 mm due to the presence of the stagnation plane. As X_{NH3} increases at φ = 0.9, the peak temperature position shifts farther from the burner plug, indicating an ignition delay caused by the higher ignition energy of NH_3 compared to H_2. The peak temperature increases from 1665 K to 1915 K, consistent with both experimental and numerical results in Ref. [35]. Although NH_3 has a lower calorific value than CH_4 [6], the temperature increase is mainly attributed to reduced heat loss, as CO_2 participates in radiative heat transfer, whereas N_2 does not. As φ increases at $X_{NH3} = 0.6$, the maximum temperature of 1865 K occurs at $\varphi = 1.0$, which corresponds to the stoichiometric air-fuel ratio. In fuel-rich cases ($\varphi > 1.0$), the peak temperature slightly decreases to approximately 1816 K. For $\varphi \geq 1.1$, only minimal changes are observed, indicating low sensitivity of the flame temperature to further increases in the equivalence ratio. Additionally, the peak temperature position initially shifts away from the burner plug and then gradually moves closer again.

3.3. NO formation characteristics

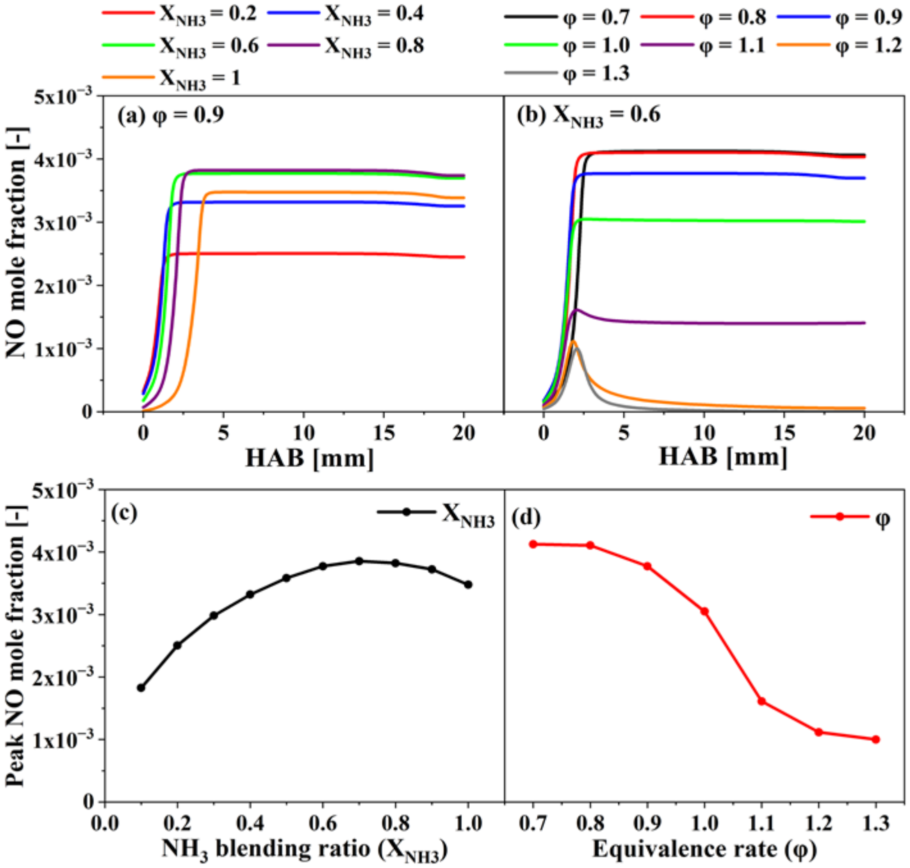

Figure 4. Mole fraction profiles of NO. (a: $\varphi = 0.9$, X_{NH3} ranges from 0.2 to 1.0, b: $X_{NH3} = 0.6$, φ ranges from 0.7 to 1.3, c: peak value with varying X_{NH3}, d: peak value with varying φ)

Fig. 4 shows the distributions and peak NO mole fractions for all cases. Most NO mole fraction profiles exhibit an increasing trend followed by stabilization as HAB increases, except for cases where $\varphi > 1.1$. With increasing X_{NH3} at $\varphi = 0.9$ in Figs. 4(a) and (c), the NO mole fraction reaches a maximum value of 3.85×10^{-3} at $X_{NH3} = 0.7$. At low X_{NH3}, the increase in NH_3 mole fraction introduces more reactive nitrogen atoms, thereby accelerating the formation rate of NO. In contrast, NH_3 promotes the conversion of NO to N_2O via reaction R842: $NH + NO = N_2O + H$ at high X_{NH3}. With increasing φ at $X_{NH3} = 0.6$ in Figs. 4(b) and (d), the peak NO mole fraction exhibits a monotonic decrease. Specifically, the NO mole fraction decreases from 4.13×10^{-3} at $\varphi = 0.7$ to 9.97×10^{-4} at $\varphi = 1.3$. At $\varphi = 0.6$, the peak NO mole fraction reaches 3.68×10^{-3}, indicating that the maximum NO mole fraction occurs within the range of $0.6 < \varphi < 0.8$. It is worth noting that the NO mole fraction profile at $\varphi > 1.1$ exhibits a peak-shaped trend in Fig. 4(b). This behavior is attributed to the continuous decrease in the mole fraction of

HNO with increasing φ, which reduces the NO formation rate via reaction R765: HNO + OH = NO + H_2O, resulting in a decreasing trend in NO mole fraction. The distributions of HNO and NH mole fractions at different X_{NH3} and φ are given in Figs B.1 and B.2 of Appendix B. A more detailed discussion is presented in the following sections.

Fig. 5 presents the peak rate of production (ROP) of key reactions governing NO formation with varying ammonia blending ratios (X_{NH3}) and equivalence ratios (φ). Specifically, reactions R763: HNO + H = NO + H_2, R765: HNO + OH = NO + H_2O, and R834: NH + O = NO + H are the main pathways responsible for NO formation. In contrast, reactions R842: NH + NO = N_2O + H, R829: NH_2 + NO = N_2 + H_2O, and R828: NH_2 + NO = NNH + OH are the dominant pathways for NO depletion.

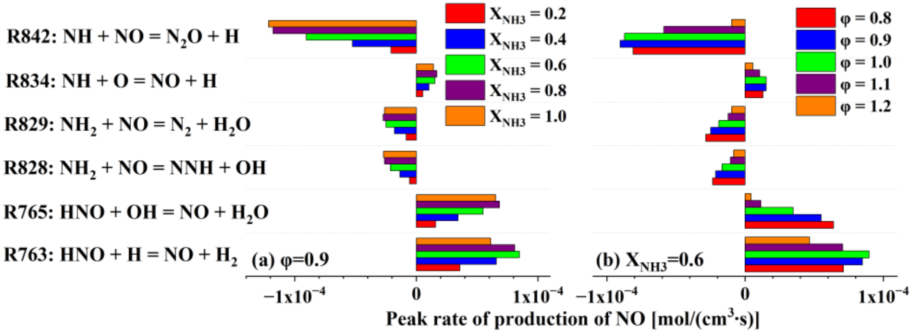

Figure 5. Peak rate of production (ROP) of key reactions governing NO formation. (a: φ = 0.9, X_{NH3} ranges from 0.2 to 1.0, b: X_{NH3} = 0.6, φ ranges from 0.8 to 1.2)

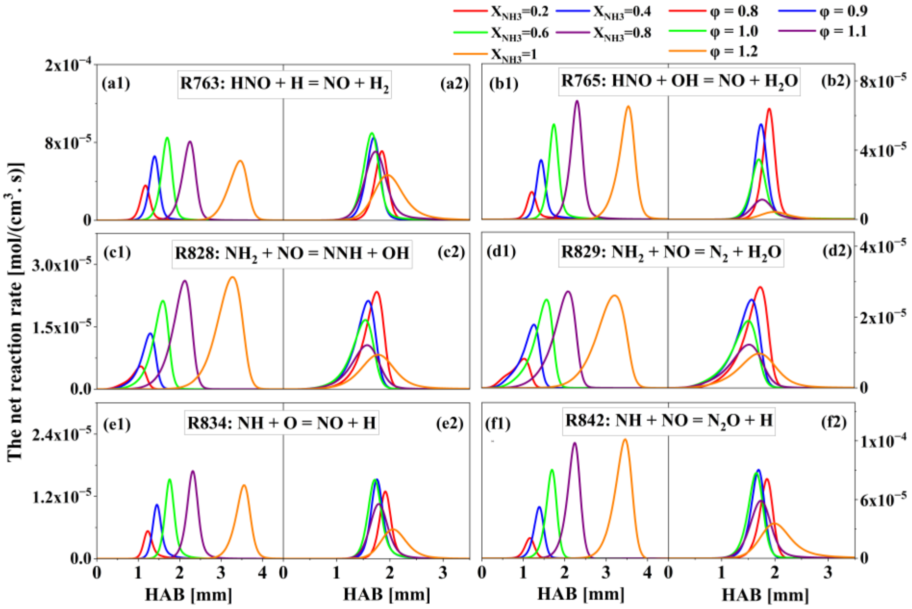

Figure 6. Net reaction rate profiles of key reactions governing NO formation. (1: φ = 0.9, X_{NH3} ranges from 0.2 to 1.0, 2: X_{NH3} = 0.6, φ ranges from 0.8 to 1.2)

Fig. 6 shows the net reaction rates of the above-mentioned reactions. With increasing X_{NH3} at φ = 0.9 in Figs. 6(a1–f1), the peak net rates of reactions R763, R765, R829, and R834 initially increase and then decrease, whereas those of R828 and R842 continuously increase. The peak rate positions of all reactions shift away from the burner plug, which is consistent with the peak temperatures in Fig. 3(a), indicating that the key reactivity of NO formation/depletion with varying X_{NH3} is strongly influenced by temperature. However, the influence of reactant mole fractions cannot be ignored. The continuous increase in HNO mole fraction with rising X_{NH3} enhances NO formation through reactions R763 and R765, allowing these reactions to dominate NO formation at low X_{NH3}. Meanwhile the continuous increase in the NH radical mole fraction with X_{NH3} enhances NO depletion via reaction R842, establishing R842 as the predominant pathway for NO depletion at high X_{NH3}.

With increasing φ at $X_{NH3} = 0.6$ in Figs. 6(a2–f2), the peak net reaction rates of reactions R763, R834, and R842 initially increase and then decrease, whereas those of reactions R765, R828, and R829 decrease monotonically. Concurrently, the peak positions of all reactions first move closer to the burner plug and then shift away. As φ increases, the HNO mole fraction continuously decreases, leading to a reduced NO formation rate through reaction R765. Meanwhile, the NH radical mole fraction initially increases and then decreases, resulting in a non-monotonic trend in the peak net rate of reaction R842. Since the change in the NO depletion rate via reaction R842 is smaller than the decrease in the NO formation rate via reactions R763 and R765, the NO mole fraction continues to decrease.

3.4. Excited radicals and their relationship to NO emission

Fig. 7 shows the peak mole fractions of NO and excited radicals at different X_{NH3} and φ values, along with the corresponding peak temperature for each case. In addition, the mole fraction distributions of OH^*/NH^*/CH^*/CO_2^*/NH_2^* radicals for all cases are shown in Fig. B.3 of Appendix B. As X_{NH3} increases at $\varphi = 0.9$, the peak mole fractions of NO, NH^*, and CH^* radicals exhibit non-monotonic behavior, with their peaks occurring at $X_{NH3} = 0.7$, 0.3, and 0.6, respectively. The peaks of OH^* and NH_2^* radicals increase monotonically with X_{NH3}, whereas CO_2^* decreases steadily. As φ increases at $X_{NH3} = 0.6$, the peak mole fractions of OH^*, NH^*, CH^*, and CO_2^* radicals initially increase and then decrease, reaching their respective peaks at $\varphi = 1.0$, 1.0, 1.0, and 0.8. In contrast, the NO mole fraction decreases consistently over the entire φ range, while NH_2^* exhibits a continuous upward trend.

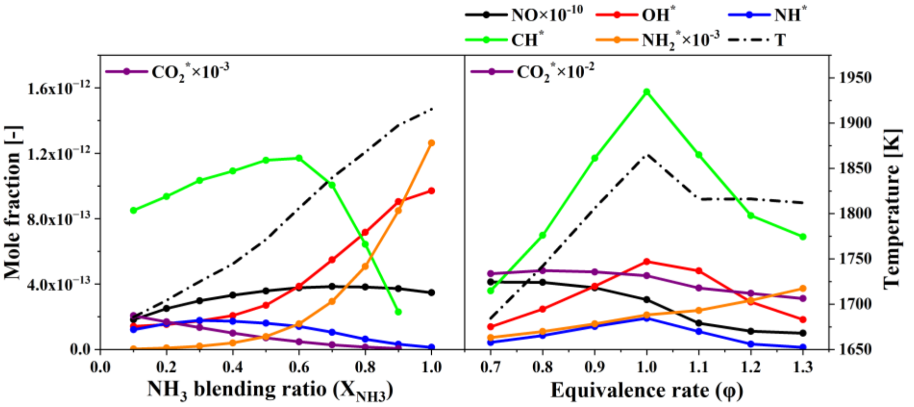

Figure 7. Peak mole fraction profiles of OH^*/NH^*/CH^*/CO_2^*/NH_2^* excited radicals. (a: varying X_{NH3}, b: varying φ)

Fig. 8 shows the relationship between the peak mole fraction of NO and those of OH^*/NH^*/CH^*/CO_2^*/NH_2^* radicals. Overall, no clear linear relationship is observed between NO and the excited radicals over the full range of X_{NH3} and φ considered. However, a nearly linear relationship ($R^2 = 0.96827$) is observed between CO_2^* and NO within the range $0.1 \leq X_{NH3} \leq 0.7$, as shown in Fig. 9(a). Notably, the NO-OH^* and NO-NH_2^* relationship profiles at varying X_{NH3} closely resemble those reported by Zhu *et al.* [19], who suggested that these profiles overlap across different φ values, indicating that OH^* and NH_2^* chemiluminescence intensities can be used to predict the NO mole fraction. Similarly, a nearly linear relationship ($R^2 = 0.98587$) is also observed between CO_2^* and NO within the range 0.8

≤ φ ≤ 1.2, as shown in Fig. 9(b). These findings reconfirm the potential of chemiluminescence for predicting NO formation/emission in NH_3-CH_4 flames, particularly using CO_2^* chemiluminescence alone.

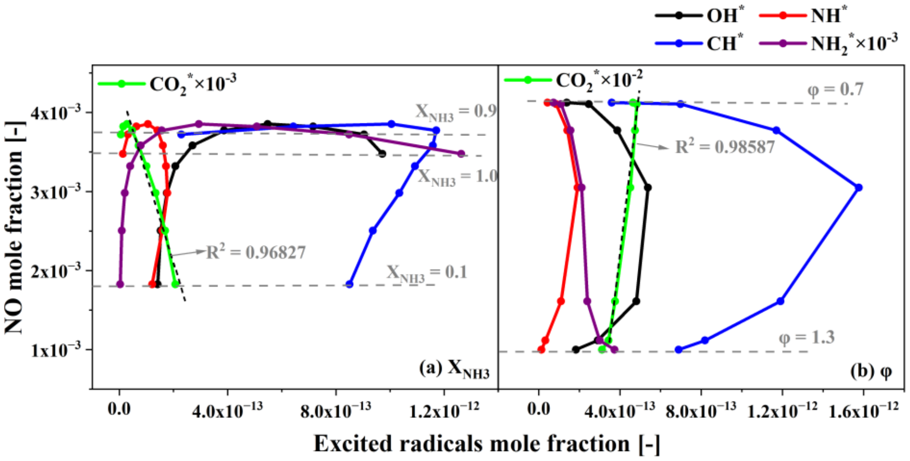

Figure 8. Relationship profiles between the mole fraction of NO and excited radicals. (a: varying X_{NH3}, b: varying φ)

To further explore the relationship between NO formation/emission and chemiluminescence, Fig. 9 presents the relationship between the peak NO mole fraction and the peak mole fraction ratios of OH^*, NH^*, CH^*, CO_2^*, and NH_2^* radicals. As X_{NH3} increases at $\varphi = 0.9$, nearly linear relationships are observed between the peak mole fraction of NO and the ratios of CO_2^*/OH^* ($R^2 = 0.99133$), CO_2^*/NH^* ($R^2 = 0.98404$), and CO_2^*/CH^* ($R^2 = 0.99761$) within the range $0.1 \leq X_{NH3} \leq 0.7$, as shown in Figs. 9 (c), (f), and (h), respectively. However, the above relationships break down at high X_{NH3}. As φ increases at $X_{NH3} = 0.6$, the ratios of CH^*/NH^*, NH_2^*/NH^*, and NH_2^*/CO_2^* all exhibit monotonic relationships with the peak mole fraction of NO, as shown in Figs. 9 (e), (g), and (j), respectively. Notably, the absolute value of the slope of the NH_2^*/CO_2^* profile is lower than those of CH^*/NH^* and NH_2^*/NH^*, indicating that the NH_2^*/CO_2^* ratio is more suitable for predicting NO formation in NH_3-CH_4 flames with varying φ, especially when considering measurement errors in chemiluminescence intensity ratios during practical application.

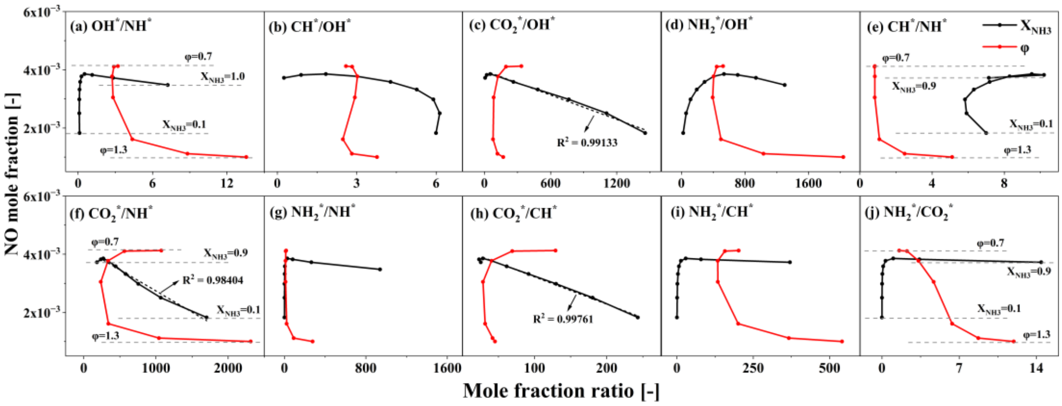

Figure 9. Relationship profiles between the mole fraction of NO and the mole fraction ratio of excited radicals. (black lines: varying X_{NH3}, red lines: varying φ)

4. Conclusions

This numerical study investigates the formation characteristics of NO in laminar NH_3-CH_4 premixed flat flames and assesses its relationship with chemiluminescence. The main findings are as follows:

(1) The applicability of the HUST-C mechanism and flame model for predicting the formation of NO and OH^*/NH^*/CH^*/CO_2^*/NH_2^* radicals in NH_3-CH_4 premixed flat flames is verified.

(2) As X_{NH3} increases, the peak temperature gradually rises, while as φ increases, it first rises and then decreases.

(3) An increase in X_{NH3} causes the NO mole fraction to first increase and then decrease because the changes in the mole fraction of HNO and NH affect the competition among key reactions R763: $HNO + H = NO + H_2$, R765: $HNO + OH = NO + H_2O$, and R842: $NH + NO = N_2O + H$. Additionally, increasing φ continuously reduces the formation rate of NO by R765.

(4) As X_{NH3} increases, the peak mole fractions of NH^* and CH^* radicals occur at $X_{NH3} = 0.3$ and 0.6, respectively; OH^* and NH_2^* increase monotonically, while CO_2^* decreases monotonically. As φ increase, the peak mole fractions of OH^*, NH^*, CH^*, and CO_2^* radicals occur at φ = 1.0, 1.0, 1.0, and 0.8, respectively, while NH_2^* shows an upward trend.

(5) A nearly monotonic relationship is observed between the peak mole fraction of NO and CO_2^*. With varying X_{NH3}, similar relationships exist between NO and the ratios of CO_2^*/OH^*, CO_2^*/NH^*, and CO_2^*/CH^*, but these relationships break down at high X_{NH3}. Over a wide range of φ, the NH_2^*/CO_2^* ratio shows strong potential for predicting NO formation/emission.

These findings provide insights for developing high-precision monitoring technologies to quantify NO_x emissions in NH_3-blended combustion systems, thereby advancing the development of emission control strategies for practical applications.

Acknowledgment

This work was supported by the Postdoctoral Fellowship Program of CPSF under Grant Number GZC20250404 and the Key Scientific and Technological Project of Henan Province (No. 252102241009).

Appendix A. Comparison of excited radical mole fraction/chemiluminescence intensity in NH_3-CH_4-air premixed flames

The details of the NH_3-CH_4-air counterflow premixed flame model are the same as those in experimental setup of Zhu *et al*. [29]. The burner nozzle diameter and the distance between the two nozzles are both 10 mm. The temperature of the fuel and oxidant are 294 K, and the pressure is set to 1 atm. The results shown in Fig. A.1 are modeled with varying ammonia blending ratios (X_{NH3} = 0, 0.2, 0.4, and 0.6) and equivalence ratios (φ = 0.6-1.3).

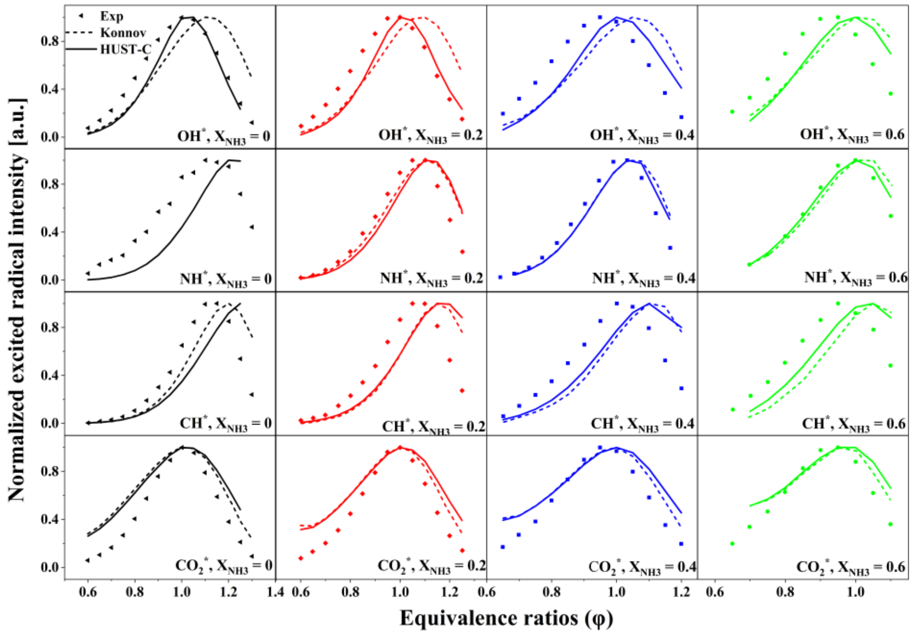

Figure A.1. Comparison of normalized OH^*/NH^*/CH^*/CO_2^* intensities at different X_{NH3} and φ in premixed counterflow flames. (Symbols represent experimental results from Zhu *et al*. [29], dashed lines correspond to numerical results from Konnov *et al*. [33], and solid lines represent numerical results from the HUST-C mechanism.)

Appendix B. Mole fraction profile of key species

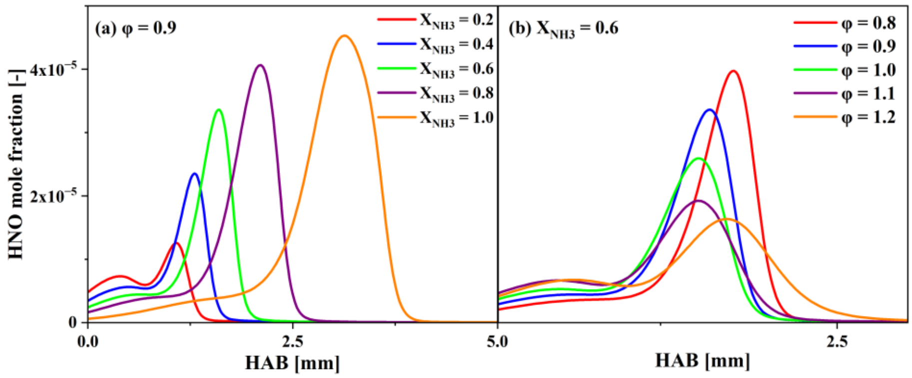

Figure B.1. Mole fraction profiles of HNO. (a: φ = 0.9, X_{NH3} ranges from 0.2 to 1.0, b: X_{NH3} = 0.6, φ ranges from 0.7 to 1.3)

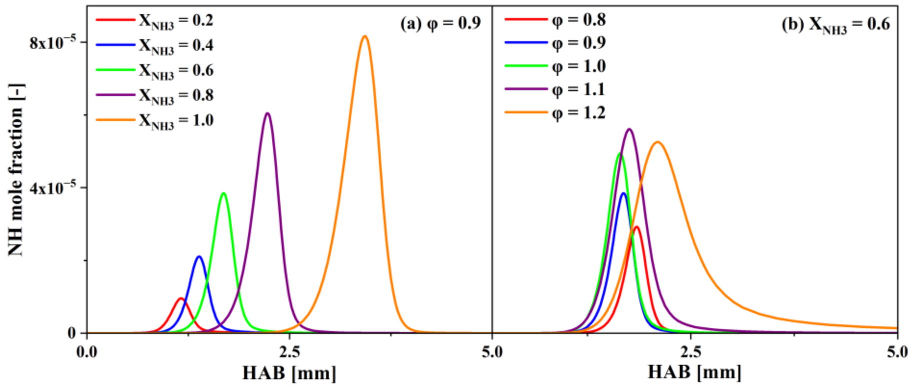

Figure B.2. Mole fraction profiles of NH. (a: φ = 0.9, X_{NH3} ranges from 0.2 to 1.0, b: X_{NH3} = 0.6, φ ranges from 0.7 to 1.3)

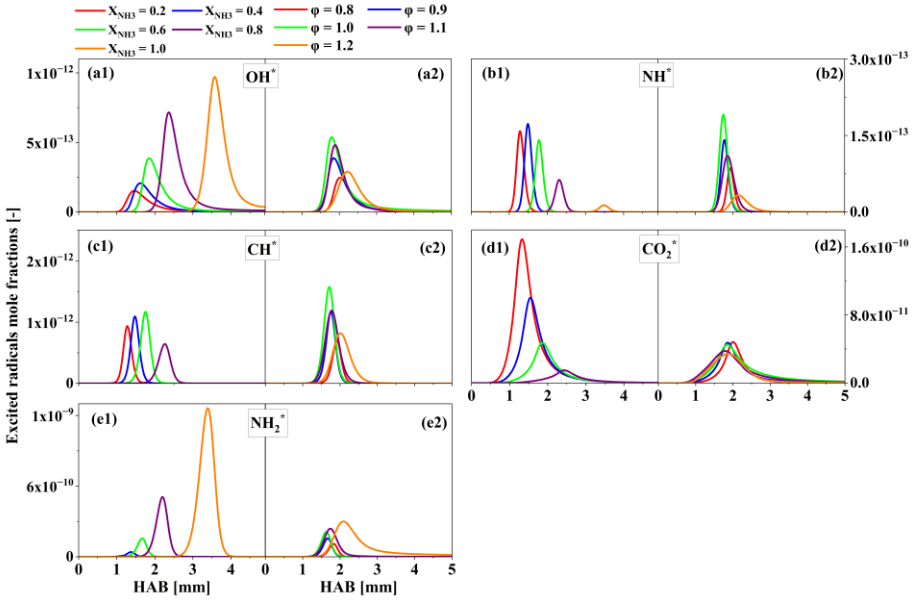

Figure B.3. Mole fraction profiles of OH^*/NH^*/CH^*/CO_2^*/NH_2^* radicals. (1: φ = 0.9, X_{NH3} ranges from 0.2 to 1.0, 2: X_{NH3} = 0.6, φ ranges from 0.8 to 1.2)

References

[1] Pitsch, H., The transition to sustainable combustion: Hydrogen- and carbon-based future fuels and methods for dealing with their challenges, *Proceedings of the Combustion Institute*, 40 (2024), 1, pp. 105638. https://doi.org/10.1016/j.proci.2024.105638.

[2] Zhang, M., *et al.*, Flame stabilization and emission characteristics of ammonia combustion in lab-scale gas turbine combustors: Recent progress and prospects, *Progress in Energy and Combustion Science*, 106 (2025), pp. 101193. https://doi.org/10.1016/j.pecs.2024.101193.

[3] Valera-Medina, A., *et al.*, Ammonia for power, *Progress in Energy and Combustion Science*, 69 (2018), pp. 63-102. https://doi.org/10.1016/j.pecs.2018.07.001.

[4] Dimitriou, P., R. Javaid, A review of ammonia as a compression ignition engine fuel, *International Journal of Hydrogen Energy*, 45 (2020), 11, pp. 7098-7118. https://doi.org/10.1016/j.ijhydene.2019.12.209.

[5] Cheng, Q., *et al*., Ammonia as a sustainable fuel: Review and novel strategies, *Renewable and Sustainable Energy Reviews*, 207 (2025), pp. 114995. https://doi.org/10.1016/j.rser.2024.114995.

[6] Kobayashi, H., *et al*., Science and technology of ammonia combustion, *Proceedings of the Combustion Institute*, 37 (2019), 1, pp. 109-133. https://doi.org/10.1016/j.proci.2018.09.029.

[7] Kumar, L., A.K. Sleiti, Systematic review on ammonia as a sustainable fuel for combustion, *Renewable and Sustainable Energy Reviews*, 202 (2024), pp. 114699. https://doi.org/10.1016/j.rser.2024.114699.

[8] Reiter, A.J., S.-C. Kong, Combustion and emissions characteristics of compression-ignition engine using dual ammonia-diesel fuel, *Fuel*, 90 (2011), 1, pp. 87-97. https://doi.org/10.1016/j.fuel.2010.07.055.

[9] Ariemma, G.B., *et al*., Ammonia/Methane combustion: Stability and NO_x emissions, *Combustion and Flame*, 241 (2022), pp. 112071. https://doi.org/10.1016/j.combustflame.2022.112071.

[10] Elbaz, A.M., *et al*., Stability and characteristics of NH_3/CH_4/air flames in a combustor fired by a double swirl stabilized burner, *Proceedings of the Combustion Institute*, 39 (2023), 4, pp. 4205-4213. https://doi.org/10.1016/j.proci.2022.06.004.

[11] Okafor, E.C., *et al*., Control of NOx and other emissions in micro gas turbine combustors fuelled with mixtures of methane and ammonia, *Combustion and Flame*, 211 (2020), pp. 406-416. https://doi.org/10.1016/j.combustflame.2019.10.012.

[12] Li, R., *et al*., Chemical mechanism development and reduction for combustion of NH3/H2/CH4 mixtures, *Fuel*, 257 (2019), pp. 116059. https://doi.org/10.1016/j.fuel.2019.116059.

[13] Ahmed, M.M.A., *et al*., Flame stabilization and pollutant emissions of turbulent ammonia and blended ammonia flames: A review of the recent experimental and numerical advances, *Fuel Communications*, 20 (2024), pp. 100127. https://doi.org/10.1016/j.jfueco.2024.100127.

[14] Somarathne, K.D.K.A., *et al*., Emission characteristics of turbulent non-premixed ammonia/air and methane/air swirl flames through a rich-lean combustor under various wall thermal boundary conditions at high pressure, *Combustion and Flame*, 210 (2019), pp. 247-261. https://doi.org/10.1016/j.combustflame.2019.08.037.

[15] Udaybhanu, G., *et al*., Experimental and numerical investigation of NH_3 flames under the influence of hot flue gases in a novel two stage porous burner, *Fuel*, 396 (2025), pp. 135395. https://doi.org/10.1016/j.fuel.2025.135395.

[16] Okafor, E.C., *et al*., Experimental and numerical study of the laminar burning velocity of CH_4–NH_3–air premixed flames, *Combustion and Flame*, 187 (2018), pp. 185-198. https://doi.org/10.1016/j.combustflame.2017.09.002.

[17] Glarborg, P., *et al*., Modeling nitrogen chemistry in combustion, *Progress in Energy and Combustion Science*, 67 (2018), pp. 31-68. https://doi.org/10.1016/j.pecs.2018.01.002.

[18] Wang, S., *et al*., Applying heat flux method to laminar burning velocity measurements of NH_3/CH_4/air at elevated pressures and kinetic modeling study, *Combustion and Flame*, 236 (2022), pp. 111788. https://doi.org/10.1016/j.combustflame.2021.111788.

[19] Zhu, X., *et al*., NO and OH* emission characteristics of very-lean to stoichiometric ammonia–hydrogen–air swirl flames, *Proceedings of the Combustion Institute*, 38 (2021), 4, pp. 5155-5162. https://doi.org/10.1016/j.proci.2020.06.275.

[20] Li, Z., *et al*., Revealing the competitive relationship between soot formation and chemiluminescence, *Combustion and Flame*, 245 (2022), pp. 112335. https://doi.org/10.1016/j.combustflame.2022.112335.

[21] Li, Z., *et al*., Investigation of soot inception limits and chemiluminescence characteristics of laminar coflow diffusion flames in C/O ratio space, *Fuel*, 327 (2022), pp. 125140. https://doi.org/10.1016/j.fuel.2022.125140.

[22] Li, Z., *et al*., Experimental investigation of the competitive relationship between soot formation and chemiluminescence in laminar ammonia-ethylene inverse diffusion flames, *Proceedings of the Combustion Institute*, 40 (2024), 1, pp. 105232. https://doi.org/10.1016/j.proci.2024.105232.

[23] Capriolo, G., *et al*., An experimental and kinetic study of $OH(A^2\Sigma^+)$ formation and quenching in ammonia-hydrogen-air flames, *Combustion and Flame*, 260 (2024), pp. 113258. https://doi.org/10.1016/j.combustflame.2023.113258.

[24] Ballester, J., T. García-Armingol, Diagnostic techniques for the monitoring and control of practical flames, *Progress in Energy and Combustion Science*, 36 (2010), 4, pp. 375-411. https://doi.org/10.1016/j.pecs.2009.11.005.

[25] Hossain, A., Y. Nakamura, A numerical study on the ability to predict the heat release rate using CH^* chemiluminescence in non-sooting counterflow diffusion flames, *Combustion and Flame*, 161 (2014), 1, pp. 162-172. https://doi.org/10.1016/j.combustflame.2013.08.021.

[26] Yan, S., *et al*., Investigation of the correlation between OH^*, CH^* chemiluminescence and heat release rate in methane inverse diffusion flame, *Energy*, 283 (2023), pp. 129162. https://doi.org/10.1016/j.energy.2023.129162.

[27] Mashruk, S., *et al*., Chemiluminescent footprint of premixed ammonia-methane-air swirling flames, *Proceedings of the Combustion Institute*, 39 (2023), 1, pp. 1415-1423. https://doi.org/10.1016/j.proci.2022.08.073.

[28] Pugh, D., *et al*., An investigation of ammonia primary flame combustor concepts for emissions reduction with OH^*, NH_2^* and NH^* chemiluminescence at elevated conditions, *Proceedings of the Combustion Institute*, 38 (2021), 4, pp. 6451-6459. https://doi.org/10.1016/j.proci.2020.06.310.

[29] Zhu, X., *et al*., Chemiluminescence signature of premixed ammonia-methane-air flames, *Combustion and Flame*, 231 (2021), pp. 111508. https://doi.org/10.1016/j.combustflame.2021.111508.

[30] Guiberti, T.F., *et al*., Chemiluminescence- and machine learning-based monitoring of premixed ammonia-methane-air flames, *Applications in Energy and Combustion Science*, 16 (2023), pp. 100212. https://doi.org/10.1016/j.jaecs.2023.100212.

[31] Liu, J., *et al*., Experimental and modeling study on the ignition delay times of ammonia/methane mixtures at high dilution and high temperatures, *Proceedings of the Combustion Institute*, 39 (2023), 4, pp. 4399-4407. https://doi.org/10.1016/j.proci.2022.07.265.

[32] Konnov, A.A., An exploratory modelling study of chemiluminescence in ammonia-fuelled flames. Part 1, *Combustion and Flame*, 253 (2023), pp. 112788. https://doi.org/10.1016/j.combustflame.2023.112788.

[33] Konnov, A.A., An exploratory modelling study of chemiluminescence in ammonia-fuelled flames. Part 2, *Combustion and Flame*, 253 (2023), pp. 112789. https://doi.org/10.1016/j.combustflame.2023.112789.

[34] Issayev, G., *et al*., Spatially resolved NH^* and OH^* profiles in ammonia-hydrogen-air counterflow diffusion flames, *Proceedings of the Combustion Institute*, 40 (2024), 1, pp. 105427. https://doi.org/10.1016/j.proci.2024.105427.

[35] Li, Q., *et al*., A comprehensive parametric study on NO and N_2O formation in ammonia-methane cofired premixed flames: Spatially resolved measurements and kinetic analysis, *Combustion and Flame*, 272 (2025), pp. 113851. https://doi.org/10.1016/j.combustflame.2024.113851.

[36] Konnov, A.A., Implementation of the NCN pathway of prompt-NO formation in the detailed reaction mechanism, *Combustion and Flame*, 156 (2009), 11, pp. 2093-2105. https://doi.org/10.1016/j.combustflame.2009.03.016.

Received: 16.5.2025.
Revised: 8.8.2025.
Accepted: 14.8.2025.